

Validation of diffusion tensor MRI in the central nervous system using light microscopy: quantitative comparison of fiber properties

A. S. Choe^{a,b,*}, I. Stepniowska^c, D. C. Colvin^a, Z. Ding^{a,b} and A. W. Anderson^{a,b}

Diffusion tensor imaging (DTI) provides an indirect measure of tissue structure on a microscopic scale. To date, DTI is the only imaging method that provides such information *in vivo*, and has proven to be a valuable tool in both research and clinical settings. In this study, we investigated the relationship between white matter structure and diffusion parameters measured by DTI. We used micrographs from light microscopy of fixed, myelin-stained brain sections as a gold standard for direct comparison with data from DTI. Relationships between microscopic tissue properties observed with light microscopy (fiber orientation, density and coherence) and fiber properties observed by DTI (tensor orientation, diffusivities and fractional anisotropy) were investigated. Agreement between the major eigenvector of the tensor and myelinated fibers was excellent in voxels with high fiber coherence. In addition, increased fiber spread was strongly associated with increased radial diffusivity ($p = 6 \times 10^{-6}$) and decreased fractional anisotropy ($p = 5 \times 10^{-8}$), and was weakly associated with decreased axial diffusivity ($p = 0.07$). Increased fiber density was associated with increased fractional anisotropy ($p = 0.03$), and weakly associated with decreased radial diffusivity ($p < 0.06$), but not with axial diffusivity ($p = 0.97$). The mean diffusivity was largely independent of fiber spread ($p = 0.24$) and fiber density ($p = 0.34$). Copyright © 2012 John Wiley & Sons, Ltd.

Keywords: diffusion tensor imaging; DTI; validation; histology; myelin; registration

INTRODUCTION

Diffusion tensor imaging (DTI) is rapidly becoming a mainstay of neuroimaging studies. It has been used to characterize white matter lesions in individuals (1–5) and to quantify group differences on a voxel-by-voxel basis across the entire brain (6–8). DTI is also commonly used to reconstruct fiber pathways in white matter (9–12). These applications are based on the assumptions that diffusion anisotropy reflects white matter microstructure and that the principal eigenvector of the tensor approximates the orientation of fibers in a voxel. These measurements are at times complicated by factors such as partial volume averaging of nonparallel fibers (13) and image noise and artifacts (14,15), which limit the accuracy of diffusion tensor estimates. When DTI fiber tracking produces erroneous pathways, the failure is usually ascribed to these causes, and more robust tracking algorithms continue to be developed.

A number of studies have attempted to validate DTI and quantify the limitations to its accuracy under various experimental conditions. Numerical simulations of the effects of noise (14,15) and partial volume averaging (13) are in general agreement with theoretical calculations (16,17), and, similarly, numerical tests of fiber tracking algorithms have quantified pathway errors for a range of conditions (10,18). Several studies have also shown good agreement between diffusion MRI (dMRI) orientation estimates and ground truth in phantom studies (19–21). These simulation and phantom studies have provided important insights into the performance of DTI through the analysis of specific and well-characterized factors and their effects on DTI accuracy. More recently, several experimental studies involving comparisons of *ex vivo* diffusion data

and corresponding tissue structure have been conducted. These provide a more comprehensive understanding of dMRI by comparing diffusion anisotropy with tissue properties (22), such as fiber orientation distribution and fiber spread (23,24). Diffusion fiber tractography results have also been compared with known fiber pathways traced in *ex vivo* brain using an injected neural tract tracer, and showed good agreement (25).

The definition of a gold standard for fiber properties on a microscopic scale is an important component of a DTI validation experiment. Although high-resolution micrographs of stained tissue sections provide such a gold standard, manual data analysis is very labor intensive. In this study, we hypothesized that tensor diffusivities and fractional anisotropy (FA) depend on the spread and density of fibers. This hypothesis was examined using DTI

* Correspondence to: A. S. Choe, F. M. Kirby Research Center, Kennedy Krieger Institute, 707 North Broadway Street, Room G-25, Baltimore, MD 21205, USA. E-mail: annschoe@gmail.com

a A. S. Choe, D. C. Colvin, Z. Ding, A. W. Anderson
Vanderbilt University Institute of Imaging Science, Nashville, TN, USA

b A. S. Choe, Z. Ding, A. W. Anderson
Department of Biomedical Engineering, Vanderbilt University, Nashville, TN, USA

c I. Stepniowska
Department of Psychology, Vanderbilt University, Nashville, TN, USA

Abbreviations used: ABA, Adaptive Bases Algorithm; dMRI, diffusion MRI; DTI, diffusion tensor imaging; FA, fractional anisotropy; FOV, field of view; SNR, signal-to-noise ratio; T2-w, non-diffusion-weighted.

data and high-resolution histological micrographs acquired from an *ex vivo* owl monkey brain. The high-resolution micrographs were analyzed using a Fourier domain filtering method to measure fiber properties efficiently. The measurements from each dataset were then quantitatively compared for validation purposes.

MATERIALS AND METHODS

Image acquisition

All animal procedures were approved by the Vanderbilt Animal Care and Use Committee. A male owl monkey was given a lethal dose of barbiturate and perfused through the heart with buffered physiological saline. Fixation was performed by perfusing again with 4% paraformaldehyde in phosphate buffer, and then by 4% paraformaldehyde in phosphate buffer with 10% sucrose. The fixed brain was removed from the skull and kept in 30% sucrose for approximately 24 h. The brain was then transferred into a phosphate-buffered saline medium and scanned on a Varian (Palo Alto, California, United States) 9.4-T, 21-cm-bore magnet using a multislice, pulse gradient spin echo sequence ($b=0$ and 1309 s/mm^2 ; 21 diffusion-weighting directions; $TE=31.2 \text{ ms}$; $TR=17.1 \text{ s}$; image volume matrix, $128 \times 128 \times 132$; isotropic voxel resolution, 0.3 mm ; total scan time, 13 h). High-resolution acquisition of the diffusion data resulted in a low signal-to-noise ratio (SNR) of approximately six. One iteration of the anisotropic smoothing algorithm proposed by Ding *et al.* (26) was performed to improve the SNR to approximately eight. The parameters used were $\rho=2SD$ and $C=3$, where SD is the standard deviation of noise and C is a threshold parameter used to control the degree of smoothing. Non-diffusion-weighted (T2-w) images were also obtained and assembled into a three-dimensional volume dataset for registration purposes.

Twenty-four hours after imaging, the brain was embedded in dry ice and sectioned on a microtome at a thickness of $50 \mu\text{m}$ in the coronal plane. Using a Canon EOS20D (Lake Success, NY, USA) digital camera with a zoom lens of 70–300 mm, the tissue block was digitally photographed prior to cutting every third section, resulting in a through-plane resolution of $150 \mu\text{m}$. The initial in-plane resolution of the blockface images was $16 \mu\text{m}$ isotropic. The tissue sections were then stained for myelin using the silver staining method of Gallyas (27) and mounted on glass slides for light microscopy image acquisition. A Nikon DXM1200F (Melville, NY, USA) digital camera mounted on a Nikon E-800 microscope was used to take images of the stained sections at 0.5, 1, 2, 4, 10 and $20\times$ magnification, as shown in Fig. 1b–f. Figure 1a shows an FA map that corresponds to the low-resolution ($0.5\times$) micrograph shown in Fig. 1b. It should be noted that part of the temporal lobe seen at the lower right of the FA map is not observed in the corresponding micrograph, as it was discarded during histological processing.

Image registration

In order to transfer the tensors in the original MR image space to the high-resolution light microscopy image space, a multistep registration scheme was used. Figure 2 summarizes the steps of this procedure. First, the volume datasets of the DTI and blockface images were constructed. The dimensions of the DTI dataset were $128 \times 128 \times 132$ with an isotropic voxel resolution of 0.3 mm , and those of the blockface volume dataset were

downsampled to $256 \times 256 \times 222$ with a voxel resolution of $0.15 \times 0.15 \times 0.15 \text{ mm}^3$. The T2-w dataset was then registered to the blockface dataset using a combination of linear (i.e. rigid and anisotropic scaling) (28) and nonlinear (29) registration with the Adaptive Bases Algorithm (ABA). Next, a section of interest was chosen and the corresponding blockface and low-magnification ($0.5\times$) micrographs were registered in two dimensions, again using both linear and nonlinear registration with ABA.

For both sets of registrations (T2-w \rightarrow blockface, blockface \rightarrow micrograph), linear registration was performed using a mutual information-based method similar to that of Maes *et al.* (28). Partial volume interpolation was used for intensity interpolation of the transformed reference image (28). Powell's multidimensional direction set method was used to maximize the statistical dependence, employing Brent's one-dimensional optimization algorithm for line minimization (30). Powell's criterion was set to 10^{-5} , Brent's to 10^{-3} and the maximum number of iterations was set to 600. The number of bins for joint histogram calculation was set to 64×64 and three resolution levels were used. Transformation in the MRI to blockface step was performed by optimizing, first, the in-plane parameters and then the through-plane parameters. A set of in-plane transformations (two-dimensional translations only) using mutual information as a similarity measure was performed in order to find the field of view of the high-resolution micrographs within lower magnification micrographs of the same section, an example of which is shown in Fig. 1.

In addition to the linear transformations, nonlinear registration was performed using ABA for both steps (T2-w \rightarrow blockface, blockface \rightarrow micrograph). Fifteen control point levels and two resolution levels were used to determine the transformation scale and spatial resolution. Sixty-four bins were employed for joint histogram calculation and a Jacobian threshold of 0.05 was used as an optimization constraint. Optimization of a basis function was halted when the improvement of the cost function was below 0.0005.

Fiber property measurements

Diffusion imaging

Diffusion tensors were calculated using the method of Basser *et al.* (31). For each position in the target (micrograph) image space, the corresponding tensor in the DTI dataset was calculated using partial volume interpolation of the original diffusion-weighted images. In order to preserve the orientation of the tensors relative to the tissue after registration, the tensors were rotated using the preservation of principal direction reorientation strategy proposed by Alexander *et al.* (32).

Fiber information in the light micrographs is inherently two dimensional. In order to ensure that micrograph measurements of fiber properties reflect all fibers in that volume of tissue, only those voxels containing mostly in-plane fibers were selected for detailed data analysis. This was performed by selecting voxels in which diffusion was predominantly in plane. In-plane diffusion was determined by the following criteria: either the first two eigenvectors (corresponding to the largest two eigenvalues of the tensor) were nearly in the plane of the micrograph, or the principal eigenvector was nearly in the plane of the micrograph and the second and third eigenvalues were similar (the third eigenvalue at least 80% of the second) and less than 40% of the first. (In all cases, 'nearly' implies a maximum deviation of 25° .)

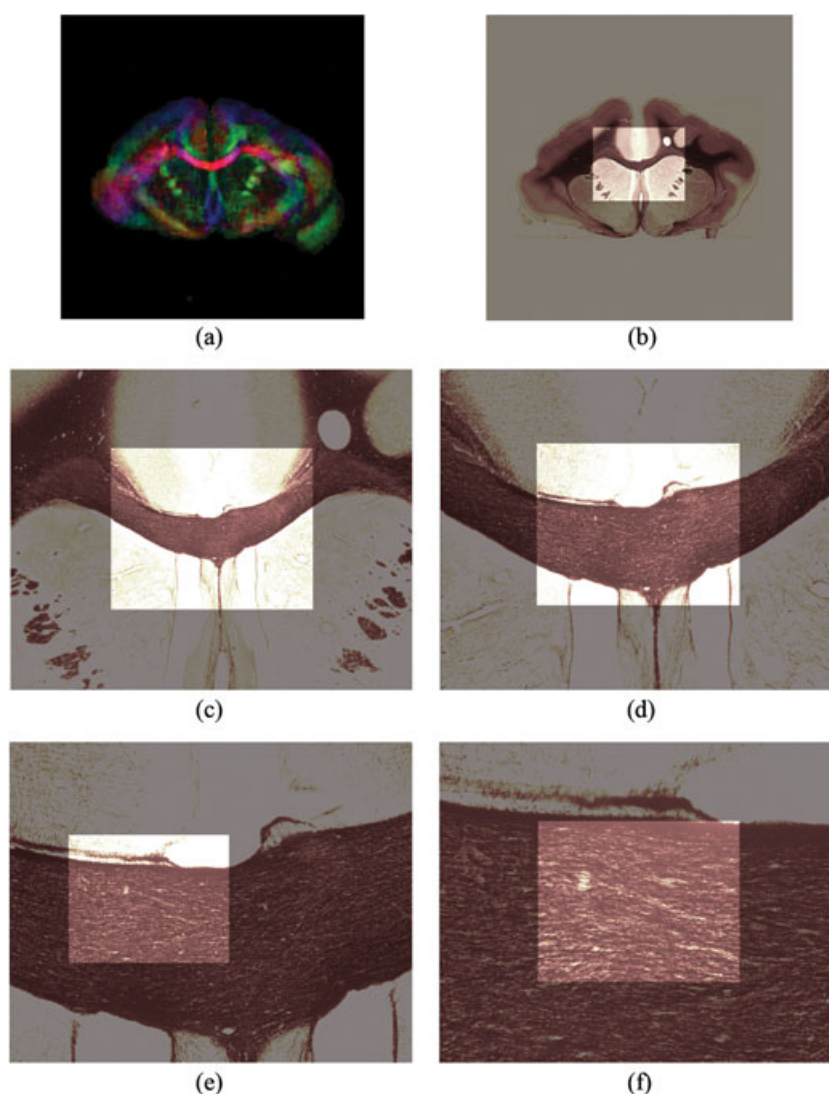


Figure 1. Iterative scheme for the localization of a high-resolution (20 \times) micrograph in a low-resolution (0.5 \times) micrograph. At each step, the location of the field of view (FOV) of the higher magnification micrograph within the lower magnification image was obtained using two-dimensional registration. (a) Fractional anisotropy (FA) map that corresponds to a low-resolution (0.5 \times) micrograph. (b) Scaled FOV of the 1 \times image is superimposed on the corresponding 0.5 \times image; (c) 2 \times FOV in the 1 \times image; (d) 4 \times FOV in the 2 \times image; (e) 10 \times FOV in the 4 \times image; (f) 20 \times FOV in the 10 \times image.

The rationale for considering the second eigenvector is that crossing fibers should lie in the plane of the first two eigenvectors (at least in the simplest model). However, if all fibers are nearly parallel and diffusion has axial symmetry around the principal eigenvector, the orientation of the second eigenvector is arbitrary (in the plane of symmetry), and so the second eigenvector should be ignored in this case. Three histological sections with the least severe tissue artifacts, such as tearing and shearing, were processed. Of the initial dataset, 102 voxels (distributed across the three sections) with mostly in-plane fibers were selected for further data analysis.

The registered tensors were diagonalized in the plane of the micrograph. The principal in-plane eigenvector provided the DTI estimate of fiber orientation, projected onto the plane. In order to quantify the effect of fiber spread on diffusion anisotropy, the two-dimensional FA was found for voxels with predominantly in-plane diffusion. The two-dimensional FA was calculated using the two in-plane eigenvalues, as defined below:

$$FA_{2D} = \sqrt{2} \frac{\sqrt{(\lambda_{i1} - \bar{\lambda})^2 + (\lambda_{i2} - \bar{\lambda})^2}}{\sqrt{\lambda_{i1}^2 + \lambda_{i2}^2}} \quad [1]$$

where λ_{i1} and λ_{i2} are the first and second in-plane eigenvalues, respectively, calculated from the 2×2 matrix constructed from the original tensor by excluding the z-component terms. $\bar{\lambda}$ is the average of the two in-plane eigenvalues.

Light microscopy

The angular distribution of myelinated fibers was measured using Fourier domain filtering (33) of high-resolution micrographs (10 \times). This method is based on the fact that the two-dimensional Fourier transform of a line in image space is nonzero on a line through the origin in the Fourier domain (at an orientation orthogonal to the image space line). In our implementation, the spatial frequency spectrum of a $300 \times 300 \mu\text{m}^2$ patch of high-resolution micrograph was filtered (via multiplication) by one of 36 directional filters that

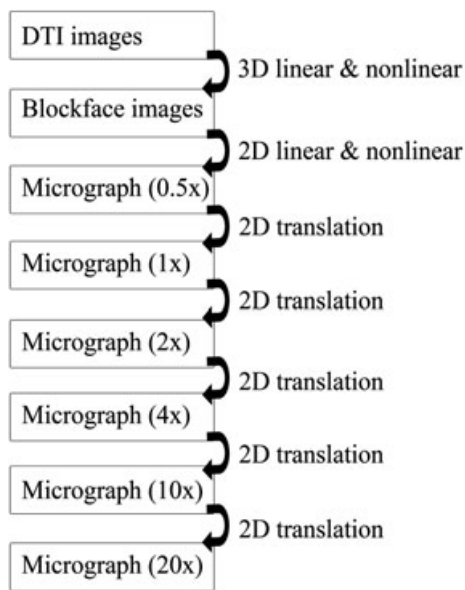


Figure 2. Registration scheme summary. Three major datasets [diffusion tensor imaging (DTI), blockface and light microscopy] were obtained. Light microscopy data were obtained under multiple magnifications, ranging from the lowest of 0.5× to the highest of 20×. The locations of the higher magnification images within the lower magnification images were found using two-dimensional registration (translations only), and the three major datasets were tied together using a combination of linear and nonlinear registration. 2D, two-dimensional; 3D, three dimensional.

pass spatial frequency components in a narrow range of angles. Each filter was designed as a function that is symmetric around the origin, forming opposing 'fan blades', 10° in width and weighted as follows (33):

$$H(f_r, \theta) = \frac{(1 - \beta f_r)}{\left\{ \left[1 + \left(\frac{f_r}{f_L} \right)^{2p} \right] \left[1 + \left(\frac{f_r}{f_H} \right)^{2q} \right] \right\}^{1/2}} \cos^\alpha \left(\frac{\theta - \theta_0}{B} \pi \right) \quad [2]$$

where β is the slope of the weighting function, f_r is the normalized radial frequency, p is the order of the high-pass filter, q is the order of the low-pass filter, f_H is the upper cut-off frequency, f_L is the lower cut-off frequency, θ is the angle of the Fourier transform sample, θ_0 is the central angle of the desired fan blade, B is the angular bandwidth and α is a weighting factor. The parameters used by Chaudhuri *et al.* (33) were also found to perform well for our experiment ($\beta=0.7$, $p=6$, $q=4$, $f_H=0.5$, $f_L=0.02$, $\alpha=0.5$ and $B=10^\circ$). An example of the directional filter for $\theta = 137.5^\circ$ is illustrated in Fig. 3.

Each filter passed spatial frequencies near the center of the blade, attenuating them more as they approached the blade edges at the center angle $\pm 5^\circ$. The 36 filter functions differed only by rotation: the center-to-center separation of neighboring blades was 5° (blades overlapped to provide more uniform sensitivity as a function of orientation).

The Fourier domain filters produced 36 component images containing fiber information at corresponding orientations. These component images were collectively thresholded, initially using the method of Otsu (34), to create binary images. The threshold value was then iteratively adjusted until the fiber pixel ratio (i.e. the ratio of pixels representing fibers over the total number of pixels) measured from a combined image (created

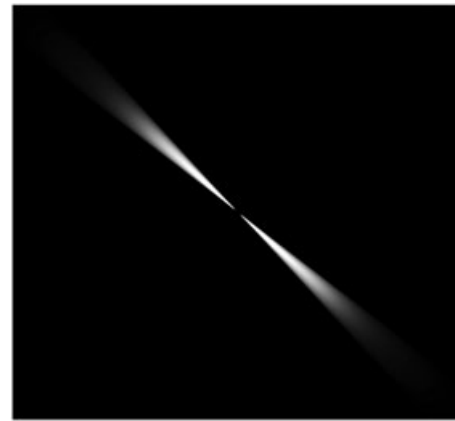


Figure 3. Composite directional filter in the Fourier domain. Each filter was designed using a combination of a fan filter, a Butterworth band-pass filter, a ramp-shaped low-pass filter and a raised cosine window. $\theta = 137.5^\circ$ and $B = 10^\circ$.

using a binary 'OR' of the 36 component images) was the same as the fiber pixel ratio measured from the original micrograph patch [calculated using the threshold of Otsu (34)]. The total number of pixels above threshold in each component image represented the fraction of fibers in the corresponding orientation, which was then used to create a fiber orientation histogram. Polar plots ('rose' plots) were used to visualize the fiber orientation histograms, which effectively display the dominant orientation and coherence of stained in-plane fibers. In the rose plot, the amplitude at a particular orientation corresponds to the fraction of fibers at that angle. The peaks of the distribution (the petals) indicate the orientations of fiber bundles, whereas the widths correspond to the degree of fiber coherence. The principal fiber orientation was calculated using a principal component analysis, and the standard deviation (relative to the principal orientation) of the fiber orientations provided a measure of angular spread. Of the 102 voxels in the final dataset, 73 were observed to have some degree of fiber crossing. Therefore, fiber crossing is a major contributor to the measured fiber spread.

A simple measure of fiber density can be taken from the fiber to nonfiber area ratio, calculated by thresholding light micrograph images. However, this method cannot discriminate between linear structures (fibers) and features with other shapes (e.g. vessels and micrograph artifacts). Similarly, a simple intensity threshold cannot account for crossing fibers in the density measurement. Ideally, the density measurement should reflect the volume fraction of fibers in the three-dimensional volume of the tissue section, and therefore should count the area of both fibers at a crossing point. In order to address these concerns, a different measure of fiber density based on the Fourier domain filtering method was utilized. A summed image for each patch of micrograph was created by thresholding and summing the 36 filtered fiber images. By adding the binary filtered images, regions of intersecting fibers are counted multiple times and each voxel in the resulting summed image represents the number of fibers detected by the filtering method at that point. Finally, the density was defined to be the average value of the summed image, calculated by summing the values of all the voxels and dividing by the total number of voxels within the image. It should be noted that, as crossing regions are counted multiple times, the density measured in this way can be greater than unity. This results from the fact that all fibers in the

tissue volume are projected onto the two-dimensional plane of the micrograph and contribute to filtered area measurements in the image. The performance of the fiber spread and density measurement using Fourier domain filtering was tested using simulated fiber micrographs, an example of which is shown in Fig. 4. A total of 100 simulated patches with varying degrees of angular distribution width (uniformly distributed between 20° and 180°), fiber density (uniformly distributed volume ratio between 0 and 0.9) and peak orientation (uniformly distributed between 0° and 180°) were analyzed using the Fourier domain filtering method. For each of the patches, the true fiber angle standard deviation and the measured fiber angle standard deviation data were compared. In addition, the true fiber density and measured fiber density were obtained and compared.

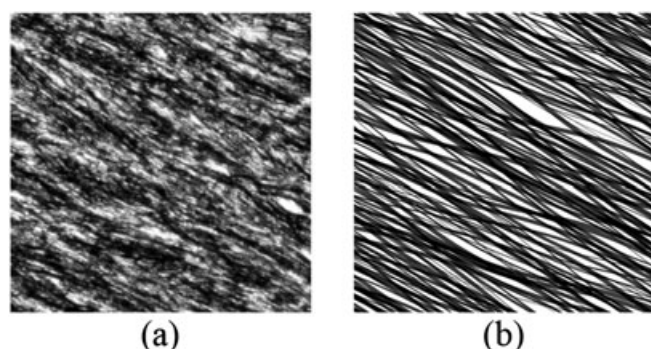


Figure 4. Actual and simulated micrograph patches. (a) A high-resolution micrograph of fibers in the corpus callosum, imaged at 20× magnification. The measured fiber orientation is 153° to the horizontal axis. (b) Simulated high-resolution micrograph of fibers. The fiber orientation was chosen at random from a normal distribution ($\mu = 153^\circ$, $\sigma = 24^\circ$).

RESULTS

Tensor transformation

The location of the high-resolution micrograph within a low-resolution (0.5×) micrograph was used to place tensors at the appropriate positions in the high-resolution micrographs. The overall alignment of the tensors with the myelin-stained fibers was very good. In a separate study of the same registration method, the accuracy of the overall MR to micrograph registration procedure was assessed by measuring the distance between 291 registered landmarks, selected in the MR image space, and the corresponding landmarks selected in the micrograph space. The average error distance of the MR data registered to micrograph data was 0.324 ± 0.277 mm (mean \pm standard deviation), or approximately the width of the MRI voxel (0.3 mm) (35). The agreement in orientation estimates within fiber bundles with strong directionality, such as the corpus callosum, was excellent, as shown in Figure 5a, b. It should be noted that each tensor is rendered as a surface for which the distance d between the origin and the surface in each direction is proportional to the water diffusivity in that direction (14,36):

$$d(\theta, \phi) = \vec{r}^T \tilde{D} \vec{r} \quad [3]$$

where θ is the polar angle, ϕ is the azimuthal angle, \tilde{D} is the diffusion tensor and \vec{r} is a unit vector in the chosen direction. The tensor surface is color coded using red, green and blue to represent right–left, anterior–posterior and superior–inferior coordinates of the surface, respectively.

Figure 5c shows a region with complex fiber structure and the corresponding tensors. It can be seen from Fig. 5c that diffusion tensors are more isotropic and provide less orientation information where fibers cross. This also implies that the tensors are

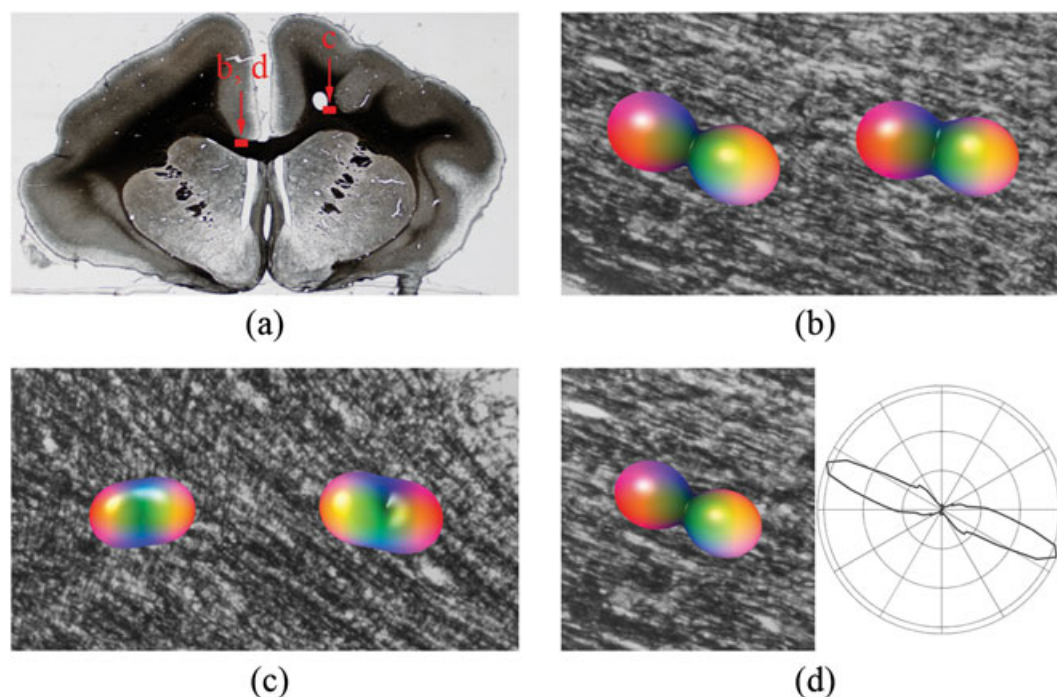


Figure 5. Tensors overlaid on light microscopy images. The registered tensors are overlaid on the corresponding high-magnification micrographs. Relative locations of the high-magnification (20×) micrographs (b) and (c) are outlined in the lower magnification (0.5×) micrograph (a). All diffusion surfaces are scaled by (in-plane) fractional anisotropy and are color coded (red, right–left; green, anterior–posterior; blue, superior–inferior). The surfaces therefore tend to be small and spherical where anisotropy is low. The fiber orientation of myelin-stained fibers on the left in (b) is visualized using a rose plot (d).

limited by the MRI spatial resolution and are unable to reflect the fine details of fiber pathways less than one voxel in diameter.

Fiber property measurements

The performance of the Fourier domain filtering method, employed to measure the angular distribution of myelinated fibers, was tested using Monte Carlo simulation. The relationship between the measured fiber spread (i.e. standard deviation) of the simulated micrograph and the true fiber spread is shown in Fig. 6a. The measured angular spread is approximately equal to the true value ($y = 0.987x + 0.009$, $R^2 = 0.998$, where y is the measured value and x is the true value). The relationship between the measured and true fiber density, shown in Fig. 6b, is linear with a slope of approximately unity ($y = 1.002x - 0.022$, $R^2 = 0.988$). These comparisons strongly suggest that the Fourier domain filtering method is a reliable tool for measuring the fiber properties of high-resolution micrographs. The filtering method on real data is demonstrated in Fig. 7, where tensor diffusion surfaces and rose plots are overlaid on high-resolution micrographs for visual comparison. Figures 7a and 7b are from a region with more coherent fibers, whereas Figs 7c and 7d are from a region with crossing groups of fibers. It can be seen that the Fourier domain filtering method is able to identify the orientations of crossing fiber groups effectively. Although the diffusion tensor model can effectively identify the orientation of coherent fiber groups shown in Fig. 7a,

it fails for the crossing fiber groups shown in Fig. 7c, i.e. the tensor surface becomes round in shape, losing any orientation information of the underlying fiber structure.

For each in-plane tensor overlaid on the high-resolution micrographs, a corresponding region of interest, a 'patch' with in-plane dimensions of the DTI pixels, was identified in the micrographs. Rose plots were used to visualize fiber orientation histograms that reveal the dominant orientation and coherence of stained fibers within each region. These were compared with the tensor registered with that region. An example of the analysis in the corpus callosum is shown in Fig. 5d. The in-plane principal eigenvector of the tensor in Fig. 5d is at 157° to the horizontal axis, and the dominant fiber orientation in the micrograph is at $153 \pm 12^\circ$. Figure 8 shows a histogram of the measured angle differences between the true fiber orientation (from high-resolution micrographs) and the fiber orientation from diffusion imaging of all the patches. The peak of the histogram indicates that, on average, tensors differ from their true fiber orientation by less than 10° (about the limit of accuracy of the Fourier filtering algorithm). As the tensors become isotropic, ambiguity in the fiber orientation measured by the first eigenvector increases and the measured angle differences may increase.

Multivariate regression analysis was performed with two-dimensional FA, two-dimensional mean diffusivity and two-dimensional diffusivities as the dependent variables, and fiber spread and density measurements as the independent

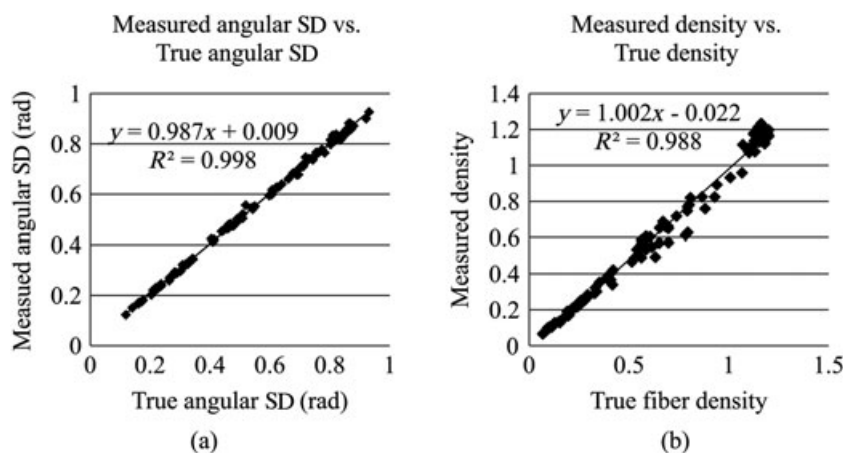


Figure 6. Performance of Fourier domain filtering method on simulated data. (a) The fiber angle standard deviation (SD) of the simulated micrographs, calculated by the Fourier domain filtering method, is plotted against the true angle SD. (b) The fiber density of simulated micrographs is plotted against the true fiber density. Both demonstrate a high correlation between true and measured data.

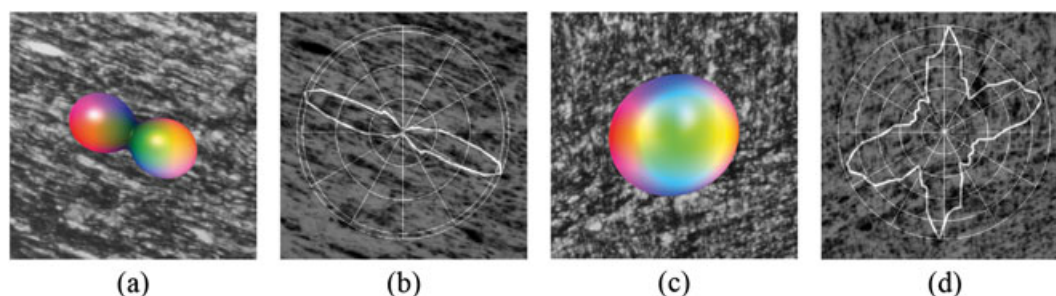


Figure 7. Examples of Fourier domain filtering method on micrographs. (a) A highly anisotropic diffusion surface is overlaid on the corresponding region of a high-resolution micrograph (with color coding: red, right-left; green, anterior-posterior; blue, superior-inferior). (b) The angular distribution of fibers in the same micrograph patch (shown in reversed contrast to make the fibers bright) is visualized using a rose plot. (c) An isotropic diffusion surface is overlaid on the corresponding micrograph patch. (d) The angular distribution of crossing fibers in the same micrograph patch as in (c) is visualized using a rose plot.

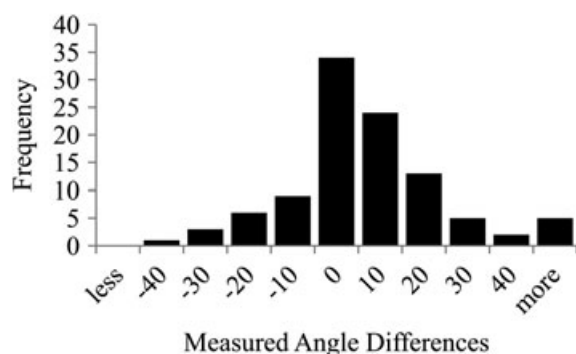


Figure 8. Histogram of the measured angle differences. The differences between the true fiber orientation measured in high-resolution light micrographs and the fiber orientation estimated from diffusion imaging are plotted (units: degrees).

variables, as shown in Table 1. Semipartial correlation coefficients (semipartial r or sr) for each of the independent variables were calculated to determine how much of the variance in the dependent variables is accounted for by fiber spread and fiber density separately. The semipartial correlation coefficient of two-dimensional FA with fiber spread, for example, shows the contribution of fiber spread to the two-dimensional FA, above and beyond the contribution of fiber density.

Increased fiber spread, measured as the standard deviation of fiber angles within the high-resolution micrograph, is associated with decreased FA ($p = 5 \times 10^{-8}$), and increased fiber density is associated with increased FA ($p = 0.03$). The overall F statistic

was 23.9 ($p < 0.05$). This relationship is described by the following model:

$$FA = 0.997 - 1.032 \times \text{spread} + 0.267 \times \text{density} \quad [4]$$

It should be noted that this relationship should be expected to hold only within the range of the conditions tested in this experiment (i.e. fiber spread from 0.30 to 0.90 rad and density from 0.44 to 2.53). Nevertheless, within this range, the model shows that FA has a stronger dependence on spread than on density (e.g. doubling of the spread produces a larger change in FA than does the doubling of fiber density; it should be noted, however, that the coefficient of the spread term depends on the units used to quantify angular spread). In addition, increased fiber spread was strongly associated with increased in-plane radial diffusivity ($p = 6 \times 10^{-6}$) and weakly associated with decreased axial diffusivity ($p = 0.07$). Increased fiber density was weakly associated with decreased radial diffusivity ($p < 0.06$), but not with axial diffusivity ($p = 0.97$). The mean diffusivity was largely independent of fiber spread ($p = 0.24$) and fiber density ($p = 0.34$). In Fig. 9, several micrographs with similar density or spread are shown to illustrate the relationship between FA and fiber spread and density. Figure 9a shows micrographs with similar degrees of fiber spread (0.36–0.44 rad), but varying fiber density, and their corresponding rose plots. Figure 9b shows light micrographs of similar fiber density (1.50–1.69), but varying degrees of fiber spread, and their corresponding rose plots.

DISCUSSION

The analysis of high-resolution micrographs was performed using a Fourier domain filtering method which provided an effective means to automatically extract fiber property measurements. We showed that the agreement was good between tensors derived from DTI and myelin-stained fibers analyzed via light microscopy, and the degree of diffusion anisotropy was highly correlated with the rose plot width. The analysis of fiber orientation and the angular distribution of high-resolution micrographs were simplified by principal component analysis. It should be noted that the simple linear relation in Equation [4] is approximate, and is only expected to hold over the limited range of measurements made in this study. It is not expected to be as precise as more sophisticated models that account for tissue heterogeneity (37). Nevertheless, it reveals a dependence of FA on fiber properties that agrees with intuition: FA increases with increasing fiber density and decreases with increasing spread. The constant term guarantees that FA is near unity for the highest density and lowest spread in the dataset, and that FA is near zero for the lowest density and highest spread. Models that account for nonlinear effects and more complicated fiber structure, such as fiber crossings, would facilitate more realistic interpretations of the data.

As a result of the high diffusion gradients and small voxel sizes required for high-spatial-resolution DTI, the data suffer from inherently low SNR. Possible solutions to this problem include increasing the number of signal averages and using an effective noise reduction, post-processing procedure. In order to improve our SNR, we acquired DTI images for a long time (13 h) and used the anisotropic smoothing algorithm proposed by Ding *et al.* (26). A single iteration of the algorithm was performed in order to avoid any excess smoothing and the consequent corruption of tensor orientation information.

Table 1. Regression of two-dimensional fractional anisotropy (FA) and two-dimensional diffusivities (dependent variables) versus fiber spread and fiber density (independent variables)

Variable	Model parameter	p	sr
Two-dimensional FA ^a			
Constant	0.997	6.872×10^{-26}	
Fiber spread	-1.032	5.134×10^{-8}	-0.52
Fiber density	0.267	0.0330	0.25
Two-dimensional axial diffusivity ^b			
Constant	0.800×10^{-3}	5.701×10^{-26}	
Fiber spread	-0.255×10^{-3}	0.071	-0.33
Fiber density	0.004×10^{-3}	0.971	0.10
Two-dimensional radial diffusivity ^c			
Constant	0.053×10^{-3}	0.202	
Fiber spread	0.493×10^{-3}	6.334×10^{-6}	0.31
Fiber density	-0.139×10^{-3}	0.060	-0.16
Two-dimensional mean diffusivity ^d			
Constant	0.426×10^{-3}	4.024×10^{-18}	
Fiber spread	0.118×10^{-3}	0.241	0.08
Fiber density	-0.068×10^{-3}	0.344	-0.08

^a F statistic: 23.9 ($p = 0.0306$).

^b F statistic: 3.853 ($p = 0.025$).

^c F statistic: 14.981 ($p = 2.069 \times 10^{-6}$).

^d F statistic: 0.700 ($p = 0.499$).

sr , semipartial correlation coefficient.

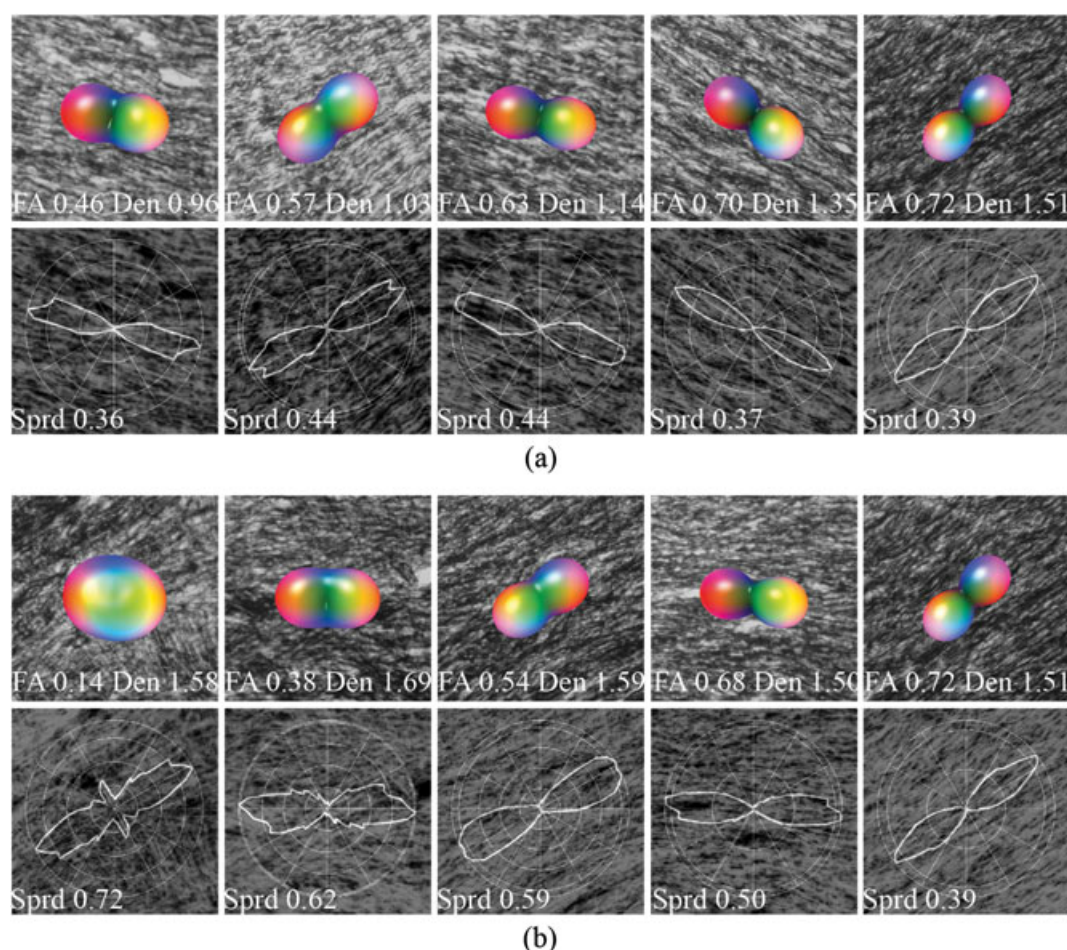


Figure 9. Example light micrographs demonstrating the relationship between fractional anisotropy (FA), fiber spread and fiber density. (a) Micrographs with similar fiber spread (0.36–0.44 rad), but varying density, are shown. As the fibers become denser, FA increases. (b) Micrographs with similar fiber density (1.50–1.69), but varying fiber spread, are shown with the corresponding rose plots. As the fibers become more coherent, FA increases.

Because the brain tissue block was sectioned, stained and mounted manually, various mounting artifacts, such as tissue tearing, folding and shearing, were inevitable. The use of nonlinear registration, especially the utilization of ABA, was essential in correcting for these mounting artifacts. The algorithm permitted spatially adaptive deformation field modeling and therefore was effective for most tissue sections. The algorithm imposes a constraint that prevents topologically incorrect registration. After registration, the fiber orientation measurements from DTI and light microscopy showed a good correlation, as observed in Fig. 8.

Our results are in general agreement with those of Leergaard *et al.* (24), although our experimental methods were quite different. First, in the study by Leergaard *et al.* (24), fiber orientations in histological sections were measured by hand. In contrast, we used an automated method based on Fourier space directional filters. Second, Leergaard *et al.* (24) used manually defined affine registration to align histological and MRI data. We used an automated registration procedure that included both affine and nonlinear transformation. These time-efficient, automated methods allowed us to analyze the correspondence of DTI and histology in a large number of voxel locations [102 *versus* 16 in the study by Leergaard *et al.* (24)]. Third, all measurements in the study by Leergaard *et al.* (24) were made in rats, whereas we studied a primate species, the owl monkey, in which white matter structure and complexity are closer to those of humans, the case of ultimate

interest. Fourth, the study by Leergaard *et al.* (24) focused on Q-ball imaging (38), using high b values ($>30\,000\text{ s/mm}^2$) and a large number of sampling directions (>500). Our study was based on more conventional acquisitions ($b \approx 1300\text{ s/mm}^2$ and 21 directions) and the tensor model, and therefore is more relevant to conventional human studies. We quantified the angular error in DTI fiber orientation estimates (comparable with the error found by Leergaard *et al.* (24) using Q-ball imaging at much higher b value) and, in addition, quantified the dependence of tensor anisotropy and eigenvalues on fiber density and coherence.

Our study has important limitations. Our measurements of fiber spread and density from high-resolution micrographs are limited to two dimensions. As in the study by Leergaard *et al.* (24), we only selected voxels with mostly in-plane diffusion for data analysis. It is shown in Table 1 and Fig. 9 that there is good correlation in these locations between the fiber properties measured by DTI and two-dimensional fiber properties measured from histological data. However, structures in the brain cannot generally be treated as two dimensional, and advancing our methods to obtain through-plane information from histological slices would greatly improve our ability to probe and compare information between DTI and histology. In addition to being dimensionally limited, our histological data lack information on other cellular properties that probably affect FA, such as axon thickness, myelination and diffusivity in the various water

compartments. The measurements of these fiber properties would allow a more comprehensive understanding of DTI.

CONCLUSION

Since the initial realization of the ability of NMR to observe molecular diffusion (39), the field has grown extensively, and DTI has become a valuable tool with applications in a wide range of diseases. Because dMRI is the only imaging method to date that can probe white matter microstructure *in vivo*, the accuracy of the information provided by the method is all the more important. However, DTI is still developing and faces a number of unsolved problems, such as the resolution of crossing fibers and the determination of how different structures interact to produce the observed DTI parameters. Having a methodology to directly compare fiber directionality and distribution measured from DTI and histological data will help to answer these questions. In this study, we developed such a methodology and demonstrated that an excellent correlation exists between the principal fiber directional measurements from DTI and myelin-stained histological sections. It was also shown that, although limited in spatial and angular resolution, DTI is able to identify (via reduced FA, for example) regions of complex fiber structure with considerable accuracy.

Acknowledgements

Financial support was obtained from the National Institutes of Health via Grant numbers 1R01NS58639, 1R01EB002777 and 1S10RR17799.

REFERENCES

- Pierpaoli C, Barnett A, Pajevic S, Chen R, Penix LR, Vitta A, Basser P. Water diffusion changes in Wallerian degeneration and their dependence on white matter architecture. *NeuroImage*, 2001; 13(6 Pt 1): 1174–1185.
- Fellgiebel A, Wille P, Muller MJ, Winterer G, Scheurich A, Vucurevic G, Schmidt LG, Stoeter P. Ultrastructural hippocampal and white matter alterations in mild cognitive impairment: a diffusion tensor imaging study. *Dement. Geriatr. Cogn. Disord.* 2004; 18(1): 101–108.
- Roberts TP, Liu F, Kassner A, Mori S, Guha A. Fiber density index correlates with reduced fractional anisotropy in white matter of patients with glioblastoma. *Am. J. Neuroradiol.* 2005; 26(9): 2183–2186.
- Warner TD, Behnke M, Eyler FD, Padgett K, Leonard C, Hou W, Garvan CW, Schmalfluss IM, Blackband SJ. Diffusion tensor imaging of frontal white matter and executive functioning in cocaine-exposed children. *Pediatrics*, 2006; 118(5): 2014–2024.
- Stahl R, Dietrich O, Teipel SJ, Hampel H, Reiser MF, Schoenberg SO. White matter damage in Alzheimer disease and mild cognitive impairment: assessment with diffusion-tensor MR imaging and parallel imaging techniques. *Radiology*, 2007; 243(2): 483–492.
- Foong J, Symms MR, Barker GJ, Maier M, Miller DH, Ron MA. Investigating regional white matter in schizophrenia using diffusion tensor imaging. *NeuroReport*, 2002; 13(3): 333–336.
- Naggara O, Oppenheim C, Rieu D, Raoux N, Rodrigo S, Dalla Barba G, Meder JF. Diffusion tensor imaging in early Alzheimer's disease. *Psychiatr. Res.* 2006; 146(3): 243–249.
- Rose SE, McMahon KL, Janke AL, O'Dowd B, de Zubicaray G, Strudwick MW, Chalk JB. Diffusion indices on magnetic resonance imaging and neuropsychological performance in amnesic mild cognitive impairment. *J. Neurol. Neurosurg. Psychiatry*, 2006; 77(10): 1122–1128.
- Conturo TE, Lori NF, Cull TS, Akbudak E, Snyder AZ, Shimony JS, McKinstry RC, Burton H, Raichle ME. Tracking neuronal fiber pathways in the living human brain. *Proc. Natl. Acad. Sci. USA*, 1999; 96(18): 10 422–10 427.
- Basser PJ, Pajevic S, Pierpaoli C, Duda J, Aldroubi A. In vivo fiber tractography using DT-MRI data. *Magn. Reson. Med.* 2000; 44(4): 625–632.
- Berman JI, Mukherjee P, Partridge SC, Miller SP, Ferriero DM, Barkovich AJ, Vigneron DB, Henry RG. Quantitative diffusion tensor MRI fiber tractography of sensorimotor white matter development in premature infants. *NeuroImage*, 2005; 27(4): 862–871.
- Catani M. Diffusion tensor magnetic resonance imaging tractography in cognitive disorders. *Curr. Opin. Neurol.* 2006; 19(6): 599–606.
- Alexander AL, Hasan KM, Lazar M, Tsuruda JS, Parker DL. Analysis of partial volume effects in diffusion-tensor MRI. *Magn. Reson. Med.* 2001; 45(5): 770–780.
- Basser PJ, Pajevic S. Statistical artifacts in diffusion tensor MRI (DT-MRI) caused by background noise. *Magn. Reson. Med.* 2000; 44(1): 41–50.
- Anderson AW. Theoretical analysis of the effects of noise on diffusion tensor imaging. *Magn. Reson. Med.* 2001; 46(6): 1174–1188.
- Jeong HK, Anderson AW. Characterizing fiber directional uncertainty in diffusion tensor MRI. *Magn. Reson. Med.* 2008; 60(6): 1408–1421.
- Koay CG, Nevo U, Chang LC, Pierpaoli C, Basser PJ. The elliptical cone of uncertainty and its normalized measures in diffusion tensor imaging. *IEEE Trans. Med. Imaging*, 2008; 27(6): 834–846.
- Lazar M, Alexander AL. An error analysis of white matter tractography methods: synthetic diffusion tensor field simulations. *NeuroImage*, 2003; 20(2): 1140–1153.
- Lin CP, Wedeen VJ, Chen JH, Yao C, Tseng WY. Validation of diffusion spectrum magnetic resonance imaging with manganese-enhanced rat optic tracts and ex vivo phantoms. *NeuroImage*, 2003; 19(3): 482–495.
- Perrin M, Poupon C, Rieul B, Leroux P, Constantinesco A, Mangin JF, LeBihan D. Validation of q-ball imaging with a diffusion fibre-crossing phantom on a clinical scanner. *Philos. Trans. R. Soc. London, B: Biol. Sci.* 2005; 360(1457): 881–891.
- Chen B, Song AW. Diffusion tensor imaging fiber tracking with local tissue property sensitivity: phantom and in vivo validation. *Magn. Reson. Imaging*, 2008; 26(1): 103–108.
- Bock AS, Olavarria JF, Leigland LA, Taber EN, Jespersen SN, Kroenke CD. Diffusion tensor imaging detects early cerebral cortex abnormalities in neuronal architecture induced by bilateral neonatal enucleation: an experimental model in the ferret. *Front. Syst. Neurosci.* 2010; 4: 149.
- Kaufman JA, Ahrens ET, Laidlaw DH, Zhang S, Allman JM. Anatomical analysis of an aye-aye brain (*Daubentonia madagascariensis*, primates: Prosimii) combining histology, structural magnetic resonance imaging, and diffusion-tensor imaging. *Anat. Rec. A, Discov. Mol. Cell Evol. Biol.* 2005; 287(1): 1026–1037.
- Leergaard TB, White NS, de Crespigny A, Bolstad I, D'Arceuil H, Bjaalie JG, Dale AM. Quantitative histological validation of diffusion MRI fiber orientation distributions in the rat brain. *PLoS One*, 2010; 5(1): e8595.
- Dauguet J, Peled S, Berezovskii V, Delzescaux T, Warfield SK, Born R, Westin CF. Comparison of fiber tracts derived from in-vivo DTI tractography with 3D histological neural tract tracer reconstruction on a macaque brain. *NeuroImage*, 2007; 37(2): 530–538.
- Ding Z, Gore JC, Anderson AW. Reduction of noise in diffusion tensor images using anisotropic smoothing. *Magn. Reson. Med.* 2005; 53(2): 485–490.
- Gallyas F. Silver staining of myelin by means of physical development. *Neurol. Res.* 1979; 1(2): 203–209.
- Maes F, Collignon A, Vandermeulen D, Marchal G, Suetens P. Multimodality image registration by maximization of mutual information. *IEEE Trans. Med. Imaging*, 1997; 16(2): 187–198.
- Rohde GK, Aldroubi A, Dawant BM. The adaptive bases algorithm for intensity-based nonrigid image registration. *IEEE Trans. Med. Imaging*, 2003; 22(11): 1470–1479.
- Press WH. *Numerical Recipes in C*. Cambridge University Press: Cambridge, 1992; 412–419.
- Basser PJ, Mattiello J, LeBihan D. Estimation of the effective self-diffusion tensor from the NMR spin echo. *J. Magn. Reson. B*, 1994; 103(3): 247–254.
- Alexander DC, Pierpaoli C, Basser PJ, Gee JC. Spatial transformations of diffusion tensor magnetic resonance images. *IEEE Trans. Med. Imaging*, 2001; 20(11): 1131–1139.
- Chaudhuri S, Nguyen H, Rangayyan RM, Walsh S, Frank CB. A Fourier domain directional filtering method for analysis of collagen alignment in ligaments. *IEEE Trans. Bio-med. Eng.* 1987; 34(7): 509–518.
- Otsu N. A threshold selection method from gray-level histograms. *IEEE Trans. Syst. Man Cybernet.* 1979; 9(1): 62–66.
- Choe AS, Gao Y, Li X, Compton KB, Stepniewska I, Anderson AW. Accuracy of image registration between MRI and light microscopy in the ex vivo brain. *Magn. Reson. Imaging*, 2011; 29(5): 683–692.
- Parker GJ. Analysis of MR diffusion weighted images. *Br. J. Radiol.* 2004; 77 (Spec No. 2): S176–S185.
- Novikov DS, Kiselev VG. Effective medium theory of a diffusion-weighted signal. *NMR Biomed.* 2010; 23(7): 682–697.
- Tuch DS, Reese TG, Wiegell MR, Wedeen VJ. Diffusion MRI of complex neural architecture. *Neuron*, 2003; 40(5): 885–895.
- Hahn EL. Spin echo. *Phys. Rev.* 1950; 80: 580–594.